

# The Effect of Post-Heat Treatment on Microstructure of 316L Cold-Sprayed Coatings and Their Corrosion Performance

B. Dikici, H. Yilmazer, I. Ozdemir, and M. Isik

(Submitted November 13, 2015; in revised form March 6, 2016)

The combined effects of process gases and post-heat treatment temperature on the microstructure of 316L cold-sprayed coatings on Al5052 substrates have been investigated in this study. The stainless steel coatings were subjected to heat treatment at four different temperatures (250, 500, 750, and 1000 °C) to study the effect of heat treatment. In addition, the corrosion performances of the coatings at different process temperatures have been compared using the potentiodynamic scanning technique. Microstructural characterization of the coatings was carried out using scanning and transmission electron microscopy and x-ray diffraction. The results of present study showed that cold-sprayed stainless steel coatings processed with helium exhibited higher corrosion resistance than those of coatings sprayed with nitrogen process gas. This could partially be attributed to the reduction in porosity level (4.9%) and improvement of particle-particle bonding. In addition, evaluation of the mechanical and microstructural properties of the coatings demonstrated that subsequent heat treatment has major influence on the deposited layers sprayed with He process gas.

**Keywords** coating, cold spray, corrosion, heat treatment, microstructure, process gas

## 1. Introduction

The cold spray process (CS), which is becoming a realistic competitor as a new spray technology, can produce superior coatings with improved properties, particularly stiffness, bond strength, and phase purity in comparison to conventional thermal spray processes (Ref 1). The process advantages make cold spraying particularly suitable for producing, surface protection against corrosion, and large metallic structures such as turbine blades, pistons, cylinders, valves, rings and bearing components, pump elements, and shafts can be repaired in place (Ref 2). It is important to emphasize that the key differences between cold and thermal spray methods are particularly the physical state of the particles, the process temperature, and gas and particle velocities. The cold spray process can be made at much lower temperatures with higher gas and particle velocities than traditional spraying methods (Ref 3). In other words, the cold spray process does not heat the powder particles

significantly and thus provides an excellent means to produce coatings with low oxide content and low thermal stresses (Ref 4). It is clear that stainless steel powders could easily build up layers in a short time on various substrates (Ref 5). This successful thick deposition of stainless steel has a strong potential to open new industrial applications especially high temperature oxidation, wear and corrosion protection (Ref 6). In addition, coarse powders and thick coating can be preferred for their protectiveness and practical applications.

Sundararajan et al. (Ref 7) studied the effect of heat treatment on the corrosion behavior of cold-sprayed SS 316L coatings in 1N HNO<sub>3</sub> solutions and showed that the cold-sprayed SS 316L coating exhibits a corrosion rate 20 times lower than mild steel substrate but 20–40 times higher than bulk SS 316L. However, the important problem with cold gas spraying of stainless steel is the presence of a high level of porosity which is inevitable especially when spraying the powder with N<sub>2</sub> gas (Ref 8). In the cold spray literature there has been little discussion of the effect of carrier gases on the corrosion properties of cold-sprayed coatings, and this offers a simple means of improving coating quality.

Stainless steel coatings with high level porosity accompanied by weak bonding between deposited particles cannot be candidates for any engineering field which requires high performance of wear (Ref 9), fatigue (Ref 4), and corrosion (Ref 10). On the other hand, a coating that contains some porosity can still be protective, provided the coating is sufficiently thick. This was investigated by Spencer and Zhang (Ref 10) by producing stainless steel coatings of varying thicknesses on Mg substrates. These two materials form a strong galvanic pair, and the corrosion behavior of this coating/substrate combination should be very sensitive to the overall quality of

**B. Dikici**, Department of Mechanical Engineering, Yuzuncu Yil University, 65080 Van, Turkey; **H. Yilmazer**, Department of Metallurgical and Materials Science Engineering, Yildiz Technical University, 34210 Istanbul, Turkey; **I. Ozdemir**, Department of Mechanical Engineering, Katip Celebi University, 35620 Izmir, Turkey; and **M. Isik**, Institute for Materials Research, Tohoku University, Sendai 980–8577, Japan. Contact e-mail: burakdikici@gmail.com.

the coating. One of the other main drawbacks of cold-sprayed stainless steel is low ductility due to the severe work hardening during deposition of the sprayed particles. When spraying austenitic stainless steels, it can also be difficult to obtain fully dense coatings due to their relatively high flow stress to the plastic deformation as a result of the high-energy impact of solid particles (Ref 2). The high strain rate of austenitic stainless steels during impact will make them resistant to plastic deformation in the cold spray process.

It is obvious that the properties of cold spray stainless steel coatings are strongly linked to controlling and optimizing the process parameters (Ref 10). It was recently shown that the porosity level of the coating significantly reduces when fine powder is used instead of coarse powder. Furthermore, a significant reduction in porosity (to <1%) can be achieved by applying a post treatment of cold gas sprayed stainless steel coating (Ref 6). On the other hand, it was shown that post-heat treatment of cold 316L sprayed layers did not increase the fatigue life of the component even with the presence of residual compressive stresses introduced during the cold spray process (Ref 4).

Investigations on the corrosion behavior of the coatings are very limited and this is the most important obstacle to the widespread use in engineering applications of cold spray coatings. Many studies only deal with the deposition characteristics of stainless steel coatings by the cold spray process. However, some defects such as pores, micro cracks, oxides produced by the spraying (Ref 10), and melted and cold particles can be found during cold spray deposition (Ref 2). Thus, to better understand the corrosion processes, the function of different phases grown in the coatings, pores, cracks formed during the solidification process, oxides, and cold particles should be considered (Ref 11). In this case electron backscatter diffraction (EBSD) and transmission electron microscope (TEM) analysis of the microstructure were successfully accomplished to characterize and correlate variations between the electrochemical properties and structural properties. Determination of the crystalline orientation, grain boundary structures, and grain size and morphology of coatings was accomplished using EBSD.

The effect of the powder carrying gas on the corrosion behavior of the cold spray coatings has not been extensively analyzed up to now. There has also been little discussion in the literature of the effect of the carrying gas on the microstructure of cold-sprayed coatings and its corrosion response. Therefore, this study covers the influence of helium (He) and nitrogen (N<sub>2</sub>) process gases and post-heat treatment temperature on the microstructure and corrosion performance of 316L cold-sprayed coatings on Al5052 substrates.

## 2. Experimental Procedure

### 2.1 Materials and Cold Spray Processing

316L stainless steel powders on Al5052 substrates were deposited using cold spray processing. Stationary High

Pressure cold gas spray equipment (Plasma Giken Co., Japan) with converging-diverging de Laval nozzle using nitrogen, and helium as impellent gas was used for coating deposition. Commercially available 316L stainless steel gas-atomized powder which is spherical in shape (Praxair, USA) was used as the feedstock (Fig. 1). The average powder particle size, as reported by the manufacturer, was 10–35  $\mu\text{m}$ . Al5052 was used as the substrate. Prior to coating deposition, the surface of the aluminum substrate was grit blasted with alumina using compressed air and then followed cleaning with acetone in order to improve its adhesion. The surface roughness (Ra) of the aluminum alloy substrates was measured as approximately 2.49 ( $\pm 0.07$ )  $\mu\text{m}$  using a SJ-301 stylus type of Mitutoyo Surface Roughness Measurement Tester. These specimens were subjected to thorough ultrasonic cleaning prior to coating deposition for better adhesion. Coatings were then deposited at the optimum conditions, i.e., a stagnation temperature of 600 °C and a stagnation pressure of (1–3) MPa. A constant stand-off distance of 20 mm was maintained for all the coatings.

### 2.2 Heat Treatment

In order to study the effect of annealing on the microstructure and microhardness of the coatings, the coating layer was cut off from the substrate by a wire erosion machine and then, heated at an identical heating rate of 30 °C/min over a wide range of temperatures (250, 500, 750, and 1000 °C) for the duration of 1 h in air. All the specimens were subjected to furnace cooling in air.

### 2.3 Hardness Tests

The hardness of the coated specimens was measured with micro Vickers hardness (HV) using a PC-controlled tester (Hardway, DMHV 1000 EDV) at a load of 100 gf for a dwell time of 15 s. Reported hardness values were an average of ten points taken from the coatings.

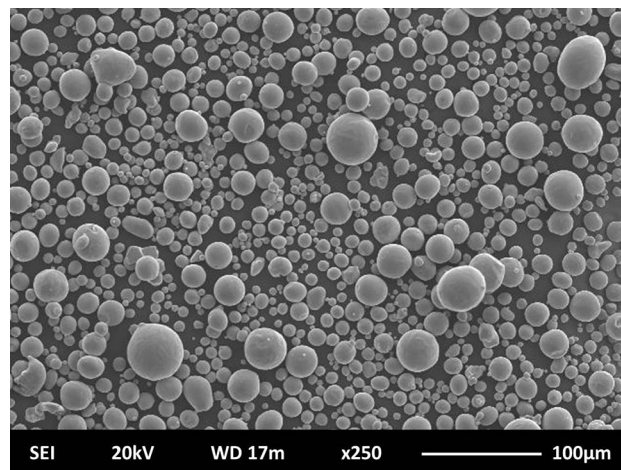


**Fig. 1** Powder morphology of 316L stainless steel used as the feedstock

## 2.4 Corrosion Tests

Electrochemical investigations of the coatings were performed with the potentiodynamic scanning (PDS) technique. All experiments were carried out with a computer-controlled potentiostat (Gamry, PCI4/750). PDS data were collected at 25, 50, and 75 °C temperatures in 3.5 wt.% NaCl solution. Ag/AgCl (in saturated KCl) and platinum (Pt) wire electrodes were used as the reference and auxiliary electrode, respectively. First, the specimens were immersed in the solution until reaching a steady open circuit potential (OCP) for beginning PDS. After equilibration, polarization was commenced at a rate of 1 mV/s. The PDS started at  $-400$  mV versus  $E_{\text{ocp}}$  and the scan was stopped when the specimens reached an anodic corrosion current density of  $100 \text{ mA/cm}^2$ . The exposed area of the test specimens was about  $10 \times 10 \text{ mm}$  ( $\pm 0.01 \text{ mm}$ ). The corrosion parameters were calculated using Echem Analyst software with the test equipment.

## 2.5 Characterization

Phase identification of the coatings was performed using an x-ray diffraction (XRD) and Cu  $K_{\alpha}$  radiation with an operating voltage of 40 kV and a tube current of 40 mA. The cross sections of the coated specimens were mounted using cold Bakelite for metallographic observations. The mounted samples were ground using wet SiC papers of up to grit #1200 in successively finer grades using an automatic polishing machine. Polishing was done using 6, 3, and 1  $\mu\text{m}$  diamond paste, respectively. This approach was used to minimize rounding of the coating/substrate interface due to the higher hardness of the coating, though sometimes as a result there were a few scratches in the Al substrates. Finally, the specimens were cleaned ultrasonically with ethanol for the microstructural observations. In order to determine the amount of porosity of deposited layers, image analysis techniques (ImageJ software) were used to quantify the porosity level from specimen's cross sections. The microstructure of the coated specimens was

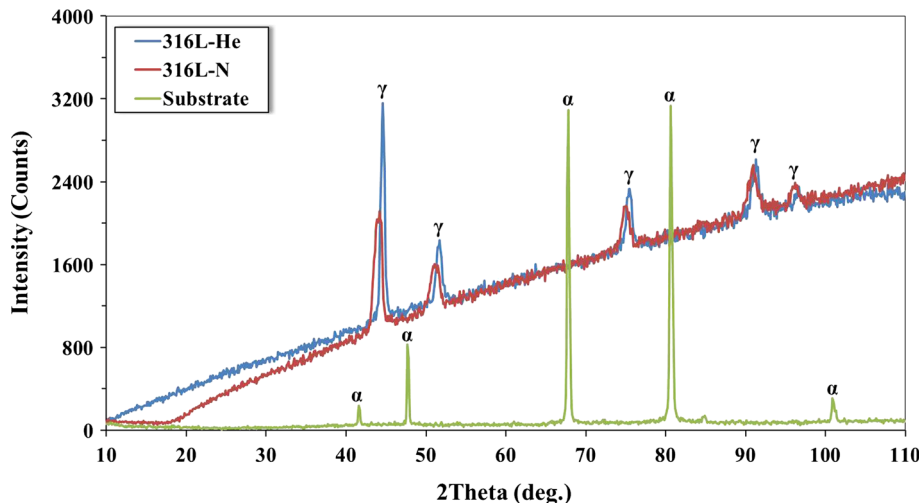
examined using a field emission scanning electron microscope (FESEM, Jeol JSM-2100F) equipped with an electron backscatter diffraction (EBSD) detector. The detailed investigation of the coating's microstructure was carried out using transmission electron microscopy (TEM) with an accelerating voltage of 200 kV. For TEM sample preparation, the disk specimen with a 3 mm diameter was wet polished to a thickness below 50  $\mu\text{m}$  using waterproof emery papers up to grit #2400. Subsequently, it was further thinned to below 20  $\mu\text{m}$  using a dimple grinder and then ion milling. Surface observation studies after the corrosion test were carried out using a SEM attached electron dispersive spectroscopy (EDS).

## 3. Results and Discussion

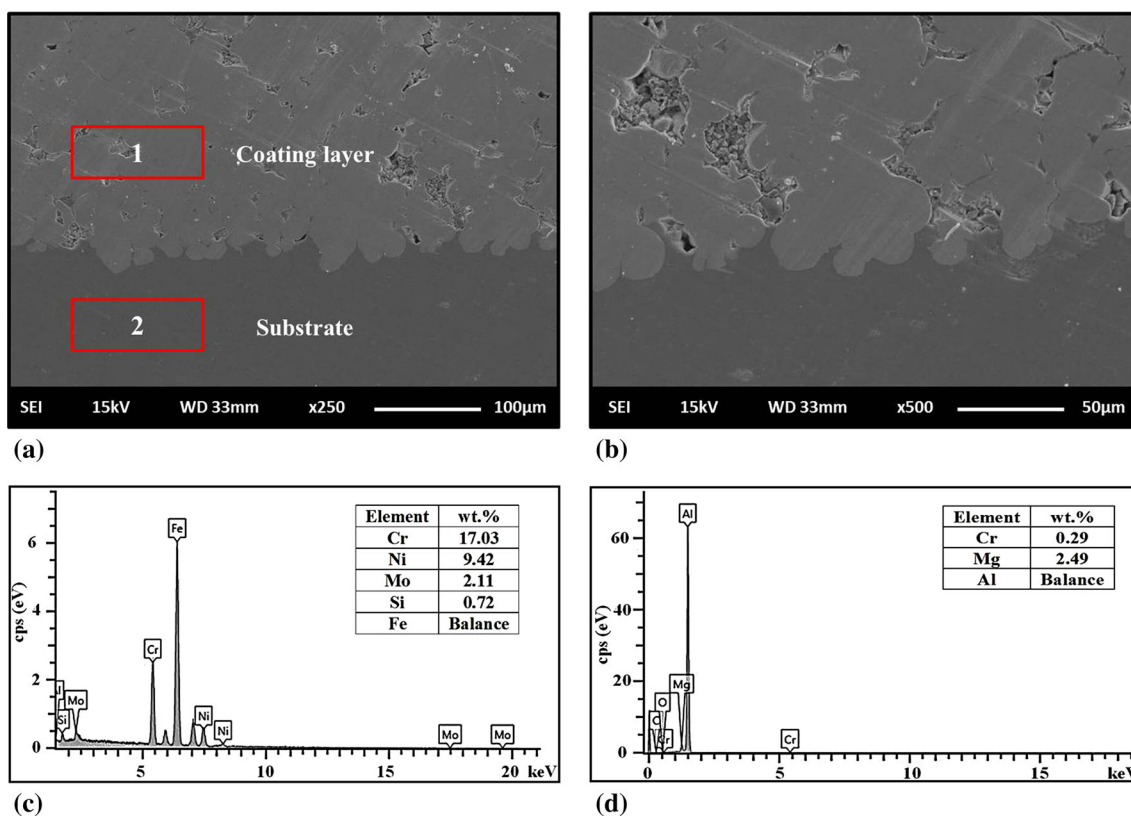
Hereafter, the 316L coatings using the carrier gases of He and  $\text{N}_2$  are referred to as '316L-He' and '316L-N' for easy expression, respectively.

Figure 2 shows the XRD patterns of cold-sprayed stainless steel coatings using He and  $\text{N}_2$  carrier gases and Al5052 substrate. It can be seen that only the austenite ( $\gamma$ ) and Al ( $\alpha$ ) phases were detected on the coatings and substrates, respectively.

Figure 3 shows the typical cross-sectional view of the cold-sprayed 316L-He and 316L-N coatings. The coating thickness of the samples was measured as  $\sim 900 \mu\text{m}$ . In the as-sprayed condition, the presence of some inter-splat voids and also the highly bonded inter-splat boundaries were evident. It is apparent that the porosity level of the cold-sprayed 316L-He coating was lower than the 316L-N coating. In fact, the porosity volume fractions of the cold-sprayed coatings were determined as  $4.9 (\pm 1.18) \text{ vol.}\%$  for the 316L-He and  $6.3 (\pm 2.16) \text{ vol.}\%$  for the 316L-N coatings, respectively. This result is in agreement with Sova et.al. (Ref 5). They reported that when spraying 316 stainless steel powder by  $\text{N}_2$  process gas porosity values were obtained 3-8% depending on particle size distribu-



**Fig. 2** XRD patterns of cold-sprayed coatings and substrate



**Fig. 3** Cross-sectional SEM images of (a) 316L-He and (b) 316L-N<sub>2</sub> coatings and EDS spectra of marked zones by (c) 1 (coating layer) and (d) 2 (substrate) in Fig. 3(a)

tion. Particle velocity is a key factor in determining the coating microstructure and properties. Higher particle velocity usually benefits to enhance the coating adhesion and cohesion strength, while decreasing porosity of the coating. Particularly, in cold spray, microstructure, adhesive strength, and deposition efficiency of the coating exhibit strong dependency to its particle velocity (Ref 12, 13). It was reported that particle impact velocities of 316 stainless steel powder cold sprayed by He gas at elevated temperature were found to be higher than that of the particles sprayed with N<sub>2</sub> process gas used (Ref 14, 15). Obviously, the lower the molecular weight of the gas the higher the velocity of the process gas (4 for He and 28 for N<sub>2</sub>). It can be said that higher particle velocity improves coating quality. Examination of the cold-sprayed microstructures shown in Fig. 3(a) and (b) generally shows that some inter-splat types of pores as well as weak inter-splat boundaries are noticeable. The difference between the coatings sprayed with N<sub>2</sub> and He process gas is that, smaller voids exist at the interfaces between deposited particles and layers more successfully bond to each other with higher adhesion when the He process gas is used. The typical elemental analysis of both substrate and coating layers are given in Fig. 3(c) and (d).

The microstructures of cold-sprayed stainless steel with higher magnification are given in Fig. 4. The austenitic stainless steel is work-hardened significantly during cold working. For this reason, strain hardening of cold-sprayed

deposits with He is more pronounced as a result of more flattening of particles upon impact (Fig. 4). Mainly, it was found that clean surfaces and good adhesion were achieved for particle/substrate bonding. Likewise, in contrast to the observations in the coating sprayed with He gas (Fig. 4a), some regional clusters of pores located in the vicinity of the layers exist in the coating sprayed with N<sub>2</sub> process gas (Fig. 4b). A higher magnification sectional view of the stainless steel coatings is presented in Fig. 4(c) and (d). A good bonding between the deposited layers and the substrate is also evident from these micrographs. There are discontinuous regions of porosity concentrated in the region between successive layers when the material is sprayed using N<sub>2</sub> gas. In contrast, the coating sprayed using N<sub>2</sub> gas is less dense than the coating sprayed using He gas. In addition, it was shown that some particles changed from spherical to slightly elongated form due to the impact velocity during the coating process (Fig. 4c). However, the stainless steel particles have not been deformed after the cold spray deposition (Fig. 4d). The higher kinetic energy on impact results in more deformation. According to literature, 640 m/s is critical deposition velocity for 316L stainless steel powder (Ref 16, 17). Additionally, the as-sprayed 316L-He coating with hardness values higher than the deposit sprayed with N<sub>2</sub> gas approved that strain-hardening effect during deposition of high velocity particles was achieved. Conversely, the observation of gradient porosity for the thick coating

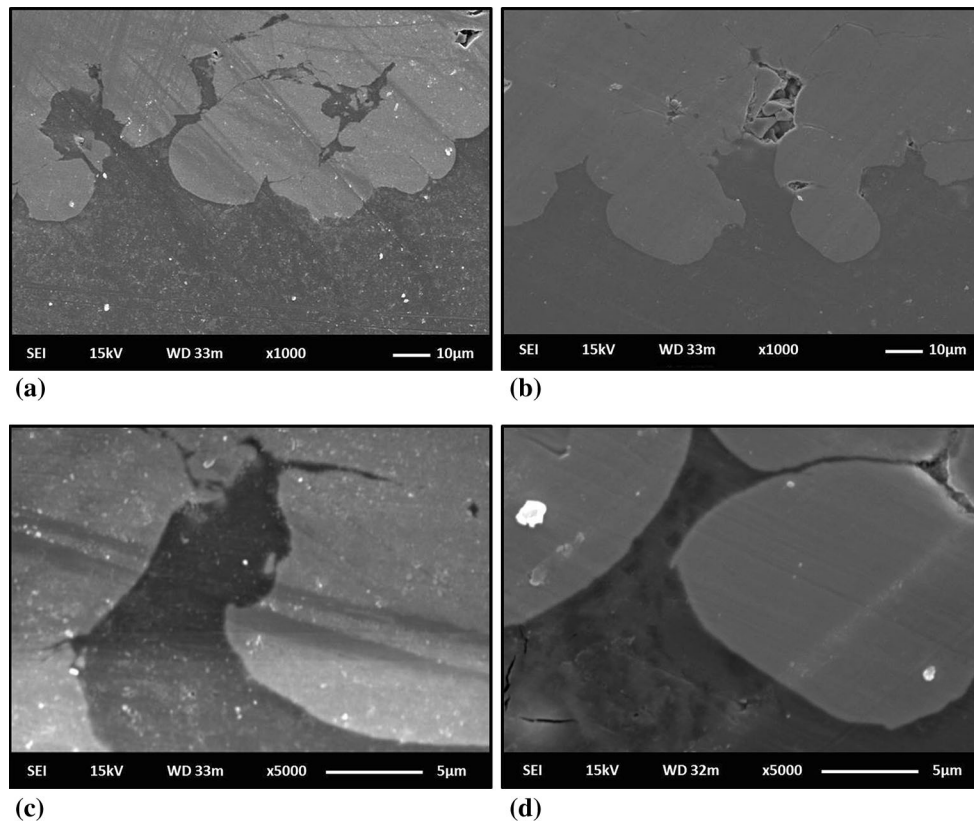


**Fig. 4** Cross-sectional SEM images of (a-c) 316L-He and (b-d) 316L-N coatings at higher magnifications

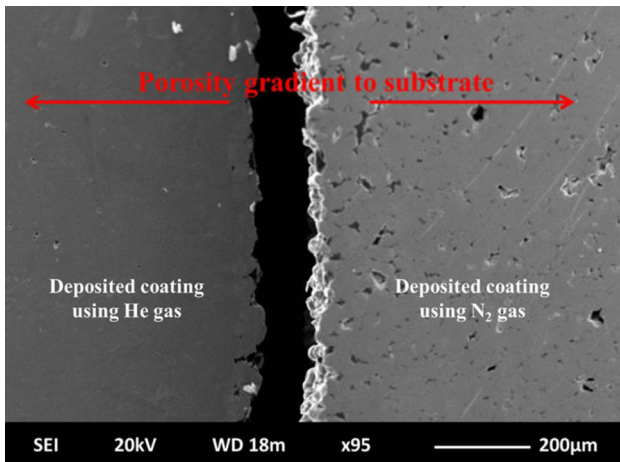


**Fig. 5** Porosity gradient throughout the coatings

sprayed with  $N_2$  demonstrated that work hardening process be partially achieved in this type of coating (Fig. 5).

Figure 6 shows the EBSD images of the cold-sprayed coatings. As seen from the orientation and grain maps, the microstructure of both 316L-He and 316L-N coatings consists of coarse and fine equiaxed grains which show a random orientation (Fig. 6a and d). Furthermore, while the fine grains show a submicron morphology with a diameter of several hundred nanometers for 316L-He, the

microstructure of 316L-N exhibits larger fine grains with a diameter of approximately  $1.3 \mu\text{m}$ . Also, the coarse grains exhibit a diameter of approximately  $11 \mu\text{m}$  in the 316L-He. Furthermore, the phase maps (Fig. 6c and d) reveal that the microstructures of both the 316L-He and 316L-N specimens consist of single FCC austenite phases, as is consistent with XRD analysis.

Figure 7 shows the maps of low-angle ( $5^\circ$ – $15^\circ$ ) and high-angle ( $15^\circ$ – $180^\circ$ ) grain boundaries (LABs and HABs) defined by green and blue lines and their volume fraction for 316L-He and 316L-N.

The histogram in Figure 7(c) reveals that while 316L-N coating shows equally mixed LABs and HABs, the volume fraction of HABs is slightly higher than that of LABs for 316L-He coating. It can be said that the size of crystallites, which indicate subgrains, is greatly reduced after cold spray deposition by He carrying gas. These results indicate that the He carrier enhanced straining during coating and consequently improved the microstructural refinement for 316 L coatings.

TEM images of the samples are presented in Fig. 8. Figure 8(a) shows the TEM bright field image of 316L-He and its selected area electron diffraction patterns from the zones, marked by 1 and 2 zones, having fine and coarse grains. Consistent with the EBSD analysis of 316L-He in Fig. 6, the bright field image of the 316L-He coating shows the existence of both coarse and fine grains. Complete Debye rings indicate that the fine grain exhibited high-



**Fig. 6** (a, d) EBSD orientation map with inverse pole figure (IPF) images, (b, e) grain maps, and (c, f) phase maps of 316L-He and 316L-N coatings, respectively

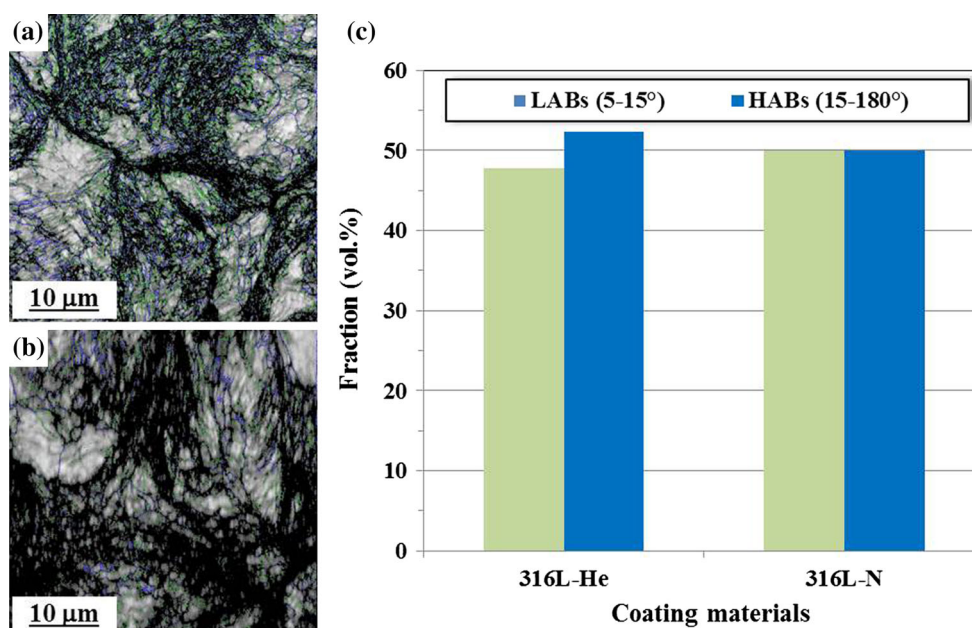


**Fig. 7** Grain boundary maps for (a) 316L-He and (b) 316L-N coatings, and (c) volume fractions of low- and high-angle grain boundaries (LABs and HABs)

angle misorientation. The contrast in the bright field images indicates a high dislocation density. The TEM bright field image of 316L-N coating and its SAED pattern are shown in Fig. 8(b). The bright field image with various contrasts indicates coarse grains having high dislocation density. Likewise, in the SAED pattern having a partial ring pattern in Fig. 8(b), both coarse and fine grains were noticeable for the 316L-N coating.

Figure 9 shows the effect of annealing temperature on the microstructure of the coatings. After the heat treatment was carried out, especially at a temperature range of 250-500 °C, almost no significant change in the porosity level of the sprayed coatings was observed. On the other hand, it should be noted that the post-heat treatment process even at high temperatures in the range of 500-1000 °C decreases the level of porosity consider-

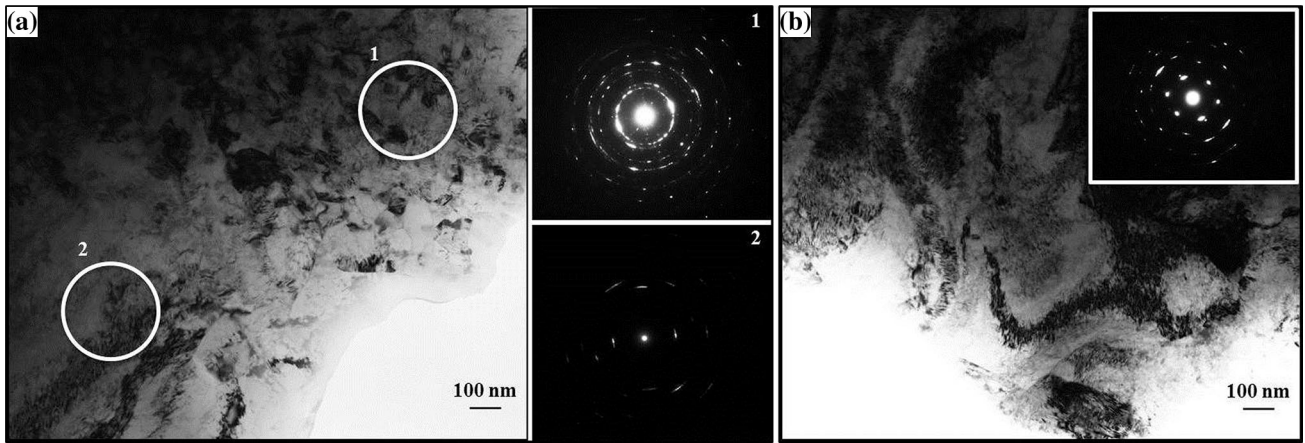


**Fig. 8** TEM bright field images and selected area diffraction patterns of (a) 316L-He and (b) 316L-N coatings

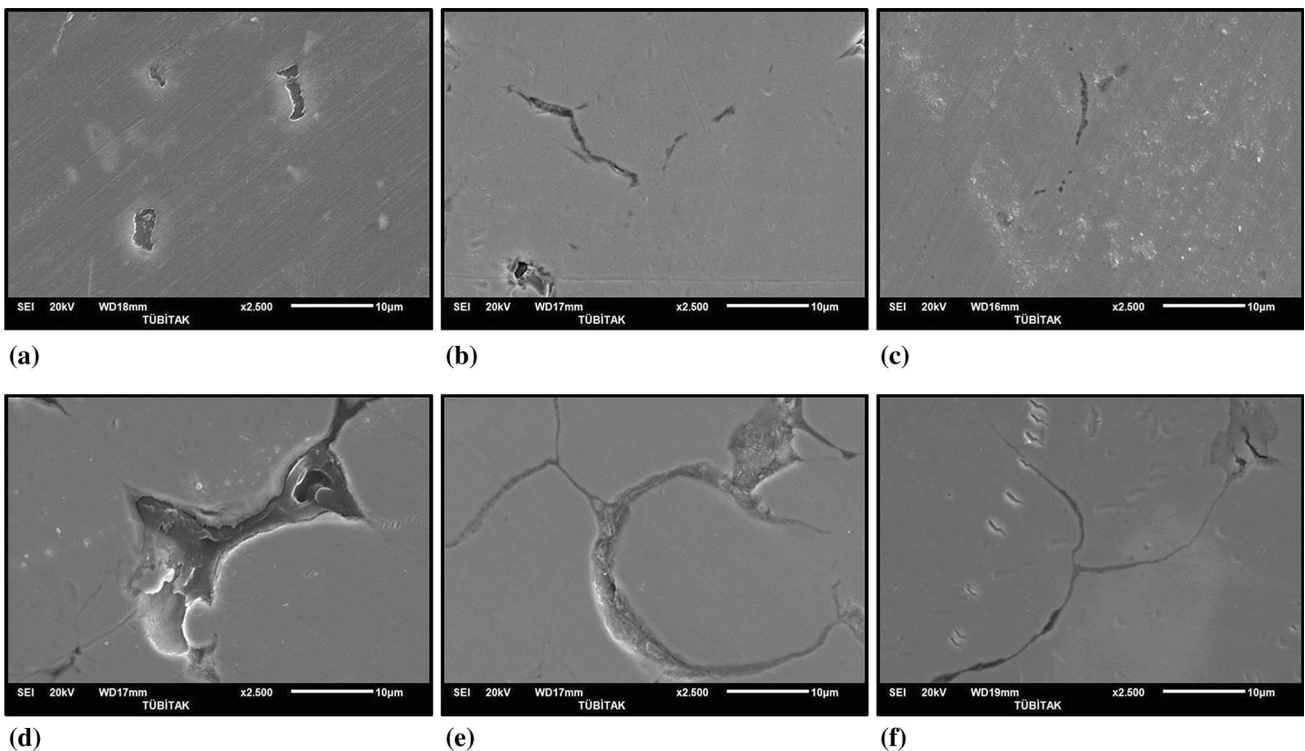


**Fig. 9** Microstructures after annealing treatment at (a, d) 500, (b, e) 750, and (c, f) 1000 °C temperatures for 316L-He and 316L-N coatings, respectively

ably (Fig. 9). These observations are also in agreement with the studies of Sundararajan et al. (Ref 7) and Meng et al. (Ref 18). In the present work, the observed low porosity in the coatings heat treated from 500 to 1000 °C can be explained by effective solid state diffusion resulting in strong intimate contact and bonding between sprayed particles. Therefore, an improvement in mechanical properties can be expected with the increasing post-heat treatment temperature. However, better interfacial bonding and also a reduction in internal defects were achieved during annealing, and other factors

such as softening of the deposited layers and elimination of dislocation density might lead to a decrease in hardness. In fact, the results shown in Fig. 10 indicate that the hardness and porosity values of the cold-sprayed SS 316L coatings decrease continuously with increasing heat treatment temperature. The higher hardness of the 316L-He coating indicates the fine grain structure because of the high volume fraction of boundaries and the triple junctions. The decrease in hardness is largely due to tempering, the elimination of cold work effects, and subsequent recrystallization with increasing heat treat-

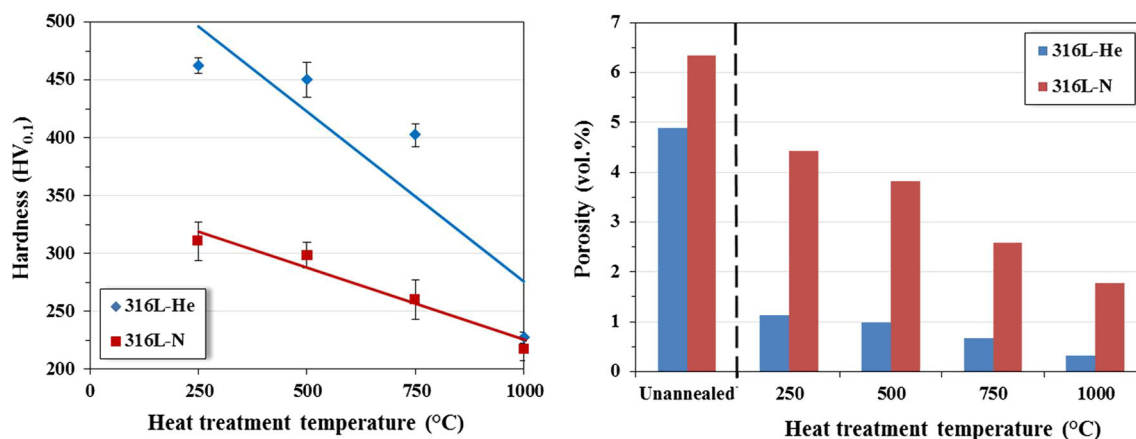


**Fig. 10** The influence of the heat treatment on the hardness and porosity values of the cold-sprayed coatings

**Table 1** Some corrosion parameters calculated from open circuit (OCP) and the potentiodynamic scanning (PDS) curves

Coating ID	Temperature, °C	$E_{ocp}$ , mV	$E_{corr}$ , mV	$E_{pit}$ , mV	$I_{corr}$ , $\mu\text{A}/\text{cm}^2$
316L-He	25	-352	-351	29	2.54
	50	-405	-411	-8	6.40
	75	-288	-715	-86	10.62
316L-N	25	-569	-498	128	5.06
	50	-629	-707	124	60.34
	75	-575	-670	-58	78.74

ment temperature, showing a more pronounced effect at higher tempering temperatures (Ref 6).

Figure 11 compares the open circuit potential (OCP) and potentiodynamic scanning (PDS) curves of the cold-sprayed 316L-He and 316L-N coatings at 25, 50, and 75 °C. In addition, some important corrosion parameters such as corrosion ( $E_{corr}$ ) and pitting ( $E_{pit}$ ) potentials and corrosion current density ( $I_{corr}$ ) values obtained from the polarization curves are given in Table 1. The parameters were calculated by the intersection of Tafel regions via the Gamry Echem Analyst program from the PDS curves of the coatings.

The OCP curves of all the studied coatings showed an abrupt potential drop at the beginning of immersion, followed by a stabilization of potential values after approximately 20 min of immersion (Fig. 11a and b). The initial potential decrease can be associated with electrochemically active species diffusing to the metal surface such as chloride adsorption, oxygen and metallic ions concentration changes, changes in the surface activity, and formation and dissolution of oxides (Ref 11). It was found that all the polarization curves of the coating materials show a higher corrosion potential than substrates. It was also noted that the coating sprayed using  $\text{N}_2$  gas presents lower corrosion resistance than the material cold sprayed using He gas at all studied temperatures (Fig. 11c and d). This behavior may be related to their higher porosity values which facilitate the electrolyte to penetrate and much more rapidly reach the substrate. The  $E_{corr}$  values of the coatings decrease with increasing test temperature (Ta-

ble 1). In other words, it was found that the corrosion resistance of the all coatings decreases with increasing test temperature and near to the Al5052 substrate resistance. Therefore, it can be said that a low porosity and a low oxidation are very important for a corrosion-resistant stainless steel coating (Ref 16).

The effects of corrosion behavior are also important when the microstructure is considered as a corrosion response. Figure 12(a) demonstrates the nucleation of pits in 316L-He coating which has been exposed to just above  $E_{corr}$ . It can be seen that, the corrosion starts at the inter-splat porosities and boundaries in the coatings. Then, the polarization behavior is influenced not only by the existing voids in the coating layer, but also by the quality of inter-particle bonding. The porosities on the metal surface are areas where the electrolyte is stagnating and because of this, the oxide film formed at the surface prevents the oxygen entering the coating. These porosities will be filled with corrosion products and passivate the upper surface by increasing the potential (Fig. 12b). The high positive charge concentration at the covered areas will attract the  $\text{Cl}^-$  ions and thus the  $\text{Cl}^-$  ion concentration in the oxide film will increase compared to other areas. Also, under these corrosion products and in the absence of sufficient oxygen, the corrosion will continue (Fig. 12c). Thus, these areas exhibit locally higher solubility of the oxide film and surface conductivity. The localized differentiations in the coating will progress quickly and in depth. This type of corrosion is known as pitting.



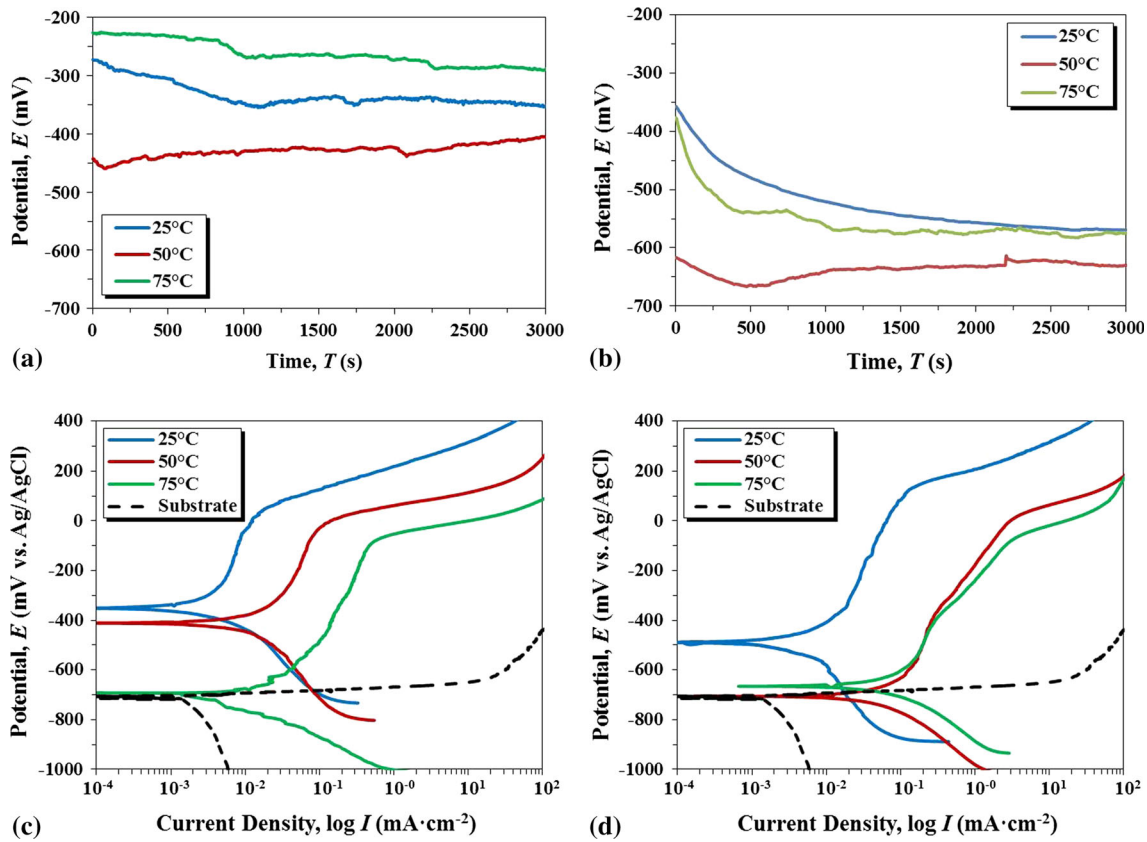


**Fig. 11** Open circuit potential (OCP) and potentiodynamic scanning (PDS) curves of cold-sprayed (a, c) 316L-He and (b, d) 316L-N coatings in aerated and unstirred 3.5% NaCl solution at 25, 50, and 75 °C temperatures

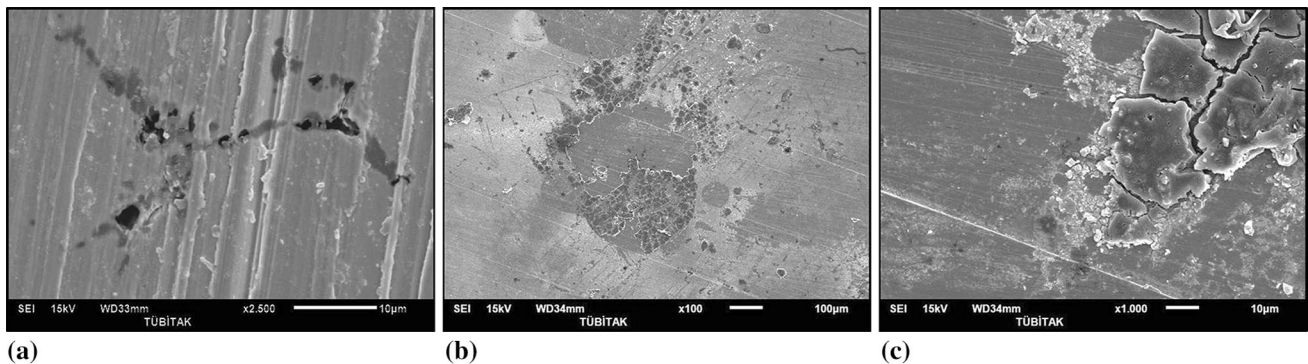


**Fig. 12** (a) Pit nucleation around inter-splat boundaries in cold-sprayed 316L-He coating, (b) and (c) oxide film formed in porosities of the 316L-N coating

Figure 13 shows SEM images of the coatings after the corrosion tests in 3.5% NaCl solution. The presence of small round pits has been observed in 316L-He coating, although there are elongated pits in 316L-N coating (Fig. 13b and f). Higher magnification images of pits can be seen in Fig. 13(c) and (g) for the cold-sprayed 316L-He and 316L-N coatings, respectively. It is possible that the electrolyte can penetrate throughout the coating layer (Ref 7). It is considered that the interiors of the inter-splat voids act as preferential areas to  $\text{Cl}^-$  ions in the solution

and this brings into existence an effect of increased corrosion of coatings on the substrate. Thus, the progression of corrosion causes a sponge-like structure in the coating layer (Fig. 13d and h). The intensity of the corroded structure in the 316L-N sample is denser than in 316L-He due to the higher porosity fraction of the sample, as shown in Fig. 13(d) and (h). Consequently, these areas will act as anode and the environment of the porosities will act as cathode. The electrolyte can reach the substrate after these defects, and a galvanic pair forms between the

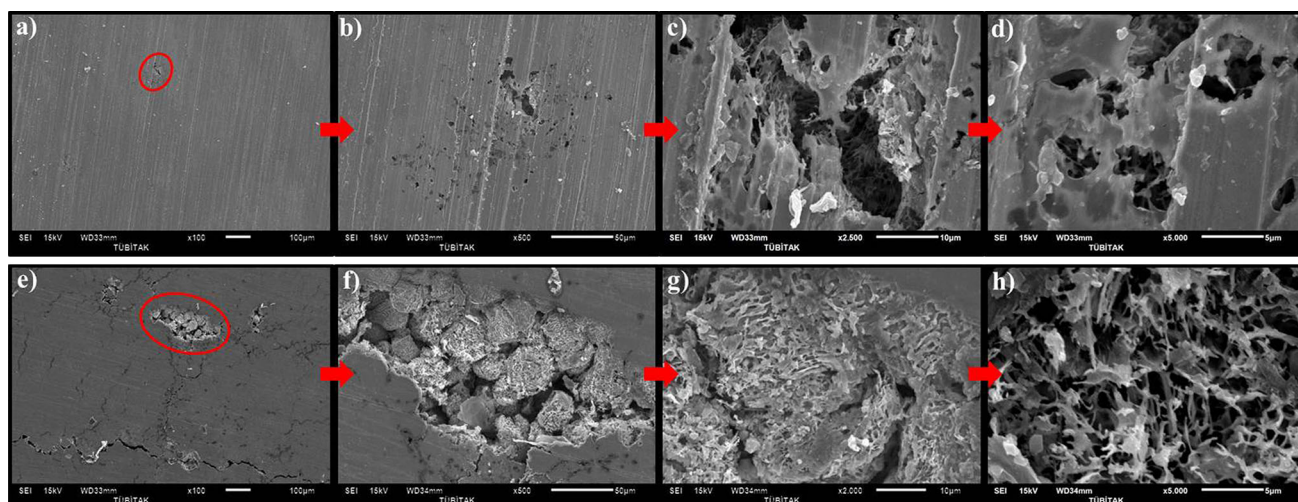


**Fig. 13** Corrosion and pit morphologies of cold-sprayed (a-d) 316L-He and (e-h) 316L-N coatings at the same magnifications

coating and substrate, thus accelerating corrosion and leading to the depletion of the coating (Ref 11). Spencer et al. (Ref 10) reported that the corrosion response of cold-sprayed 316SS approaches the behavior of bulk SS with increasing coating thickness. It was shown that thick coatings can be recommended for corrosion resistance without adhesion problems during cold deposition.

Figure 3(a) and (b) have been demonstrated that cold-sprayed 316L-He coating has less porosity and better bonding between the inter-splat particles than 316L-N coating. In other words, the coating formed using  $N_2$  carrying gas during the deposition has more weakly bonded and/or un-bonded inter-splat boundaries than 316L-He coating. It can be concluded that the coating with better inter-particle bonding and less porosity will be less subject to localized attack due to the potential differences formed between inter-splat boundaries, although the adhesion between the substrate and coating layer is good in both coatings with the same coating types and thicknesses (Ref 10). Therefore, the corrosion current density reduces significantly in the coating layer (Table 1).

#### 4. Conclusions

The combined effects of process gases and post-heat treatment temperature on the microstructure of 316L cold-sprayed coatings on Al5052 substrates have been investigated in this study. The rate and efficiency of deposition can be improved using He carrying gas. In other words, nitrogen does not work well as a powder carrying gas during 316L cold spraying. The annealing treatment both eliminates the anisotropy in the coating and heals up the incomplete interfaces between the deposited particles. It was found that the hardness and porosity values of the cold-sprayed SS 316L coatings decrease continuously with increasing heat treatment temperature. However, in the range of 250–500 °C, there is no major change in the porosity of the coatings. In addition,

both inter-splat voids and weakly bonded boundaries in the coatings deposited using He carrying gases are fewer than in the coatings deposited using  $N_2$  carrying gases. As concerns the corrosion behavior, it can be concluded that coating with better inter-particle bonding and less porosity will be less subject to localized attack, although the adhesion between the substrate and coating layer is good for the same coating thicknesses at different process temperatures.

#### Acknowledgments

The authors thank Mr. Can Sunal for the contributions.

#### References

1. S. Grigoriev, A. Okunkova, A. Sova, P. Bertrand, and I. Smurov, Cold Spraying: From Process Fundamentals Towards Advanced Applications, *Surf. Coat. Technol.*, 2014, **268**(12), p 77-84
2. A. Papyrin, V. Kosarev, S. Klinkov, A. Alkimov, and V. Fomin, Current Status of the Cold Spray Process, *Cold Spray Technology*, Chapter 5, Elsevier, New York, 2007, p 248-323
3. F. Gärtner, T. Stoltenhoff, J. Voyer, H. Kreye, S. Riekehr, and M. Kocak, Mechanical Properties of Cold-Sprayed and Thermally Sprayed Copper Coatings, *Surf. Coat. Technol.*, 2006, **200**(24), p 6770-6782
4. B. AL-Mangour, R. Dallala, F. Zhim, R. Mongrain, and S. Yue, Fatigue Behavior of Annealed Cold-Sprayed 316L Stainless Steel Coating for Biomedical Applications, *Mater. Lett.*, 2013, **91**(97), p 352-355
5. A. Sova, S. Grigoriev, A. Okunkova, and I. Smurov, Cold Spray Deposition of 316L Stainless Steel Coatings on Aluminium Surface with Following Laser Post-treatment, *Surf. Coat. Technol.*, 2013, **235**(27), p 283-289
6. B. AL-Mangour, R. Mongrain, E. Irissou, and S. Yue, Improving the Strength and Corrosion Resistance of 316L Stainless Steel for Biomedical Applications Using Cold Spray, *Surf. Coat. Technol.*, 2013, **216**(37), p 297-307
7. G. Sundararajan, P.S. Phani, A. Jyothirmayi, and R. Gundakaram, The Influence of Heat Treatment on the Microstructural, Mechanical and Corrosion Behaviour of Cold Sprayed SS 316L Coatings, *J. Mater. Sci.*, 2009, **44**(9), p 2320-2326

8. R. Maestracci, A. Sova, M. Jeandin, J.M. Malhaire, I. Movchan, P. Bertrand, and I. Smurov, Deposition of Composite Coatings by Cold Spray Using Stainless Steel 316L, Copper and Tribaloy T-700 Powder Mixtures, *Surf. Coat. Technol.*, 2016, **287**(1), p 1-8
9. M. Villa, S. Dosta, and J. Guilemany, Optimization of 316L Stainless Steel Coatings on Light Alloys Using Cold Gas Spray, *Surf. Coat. Technol.*, 2013, **235**(27), p 220-225
10. K. Spencer and M. Zhang, Optimisation of Stainless Steel Cold Spray Coatings Using Mixed Particle Size Distributions, *Surf. Coat. Technol.*, 2011, **205**(21-22), p 5135-5140
11. P. Suegama, C. Fugivara, A. Benedetti, J. Fernández, J. Delgado, and J. Guilemany, Electrochemical Behavior of Thermally Sprayed Stainless Steel Coatings in 3.4% NaCl Solution, *Corros. Sci.*, 2005, **47**(3), p 605-620
12. L. Venkatesh, N.M. Chavan, and G. Sundararajan, The Influence of Powder Particle Velocity and Microstructure on the Properties of Cold Sprayed Copper Coatings, *J. Therm. Spray Technol.*, 2011, **20**(5), p 1009-1021
13. D.L. Gilmore, R.C. Dykhuizen, R.A. Neiser, T.J. Roemer, and M.F. Smith, Particle Velocity and Deposition Efficiency in the Cold Spray Process, *J. Therm. Spray Technol.*, 1999, **8**(4), p 576-582
14. C. Borchers, T. Schmidt, F. Gärtner, and H. Kreye, High Strain Rate Deformation Microstructures of Stainless Steel 316L by Cold Spraying and Explosive Powder Compaction, *Appl. Phys. A.*, 2007, **90**(3), p 517-526
15. P. Coddet, C. Verdy, C. Coddet, F. Debray, and F. Lecouturier, Mechanical Properties of Thick 304L Stainless Steel Deposits Processed by He Cold Spray, *Surf. Coat. Technol.*, 2015, **277**(10), p 74-80
16. W.Y. Li, H. Liao, G. Douchy, and C. Coddet, Optimal Design of a Cold Spray Nozzle by Numerical Analysis of Particle Velocity and Experimental Validation with 316L Stainless Steel Powder, *Mater. Des.*, 2007, **28**(7), p 2129-2137
17. B. Sun, H. Fukunuma, and N. Ohno, Study on Stainless Steel 316L Coatings Sprayed by a Novel High Pressure HVOF, *Surf. Coat. Technol.*, 2014, **239**(9), p 58-64
18. X. Meng, J. Zhang, W. Han, J. Zhao, and Y. Liang, Influence of Annealing Treatment on the Microstructure and Mechanical Performance of Cold Sprayed 304 Stainless Steel Coating, *Appl. Surf. Sci.*, 2011, **258**(2), p 700-704